



HAL
open science

Achieving Exceptional Volumetric Desalination Capacity Using Compact MoS₂ Nanolaminates

Ting Ying, Yu Xiong, Huarong Peng, Ruijie Yang, Liang Mei, Zhen Zhang,
Weikang Zheng, Ruixin Yan, Yue Zhang, Honglu Hu, et al.

► **To cite this version:**

Ting Ying, Yu Xiong, Huarong Peng, Ruijie Yang, Liang Mei, et al.. Achieving Exceptional Volumetric Desalination Capacity Using Compact MoS₂ Nanolaminates. *Advanced Materials*, 2024, 36 (31), 10.1002/adma.202403385 . hal-04747861

HAL Id: hal-04747861

<https://hal.science/hal-04747861v1>

Submitted on 22 Oct 2024

HAL is a multi-disciplinary open access archive for the deposit and dissemination of scientific research documents, whether they are published or not. The documents may come from teaching and research institutions in France or abroad, or from public or private research centers.

L'archive ouverte pluridisciplinaire **HAL**, est destinée au dépôt et à la diffusion de documents scientifiques de niveau recherche, publiés ou non, émanant des établissements d'enseignement et de recherche français ou étrangers, des laboratoires publics ou privés.

Achieving Exceptional Volumetric Desalination Capacity Using Compact MoS₂ Nanolaminates

Ting Ying, Yu Xiong, Huarong Peng, Ruijie Yang, Liang Mei, Zhen Zhang, Weikang Zheng, Ruixin Yan, Yue Zhang, Honglu Hu, Chen Ma, Ye Chen, Xingtao Xu, Juan Yang, Damien Voiry, Chuyang Y. Tang, Jun Fan, and Zhiyuan Zeng*

Capacitive deionization (CDI) has emerged as a promising technology for freshwater recovery from low-salinity brackish water. It is still inapplicable in specific scenarios (e.g., households, islands, or offshore platforms) due to too low volumetric adsorption capacities. In this study, a high-density semi-metallic molybdenum disulfide (1T'-MoS₂) electrode with compact architecture obtained by restacking of exfoliated nanosheets, which achieve high capacitance up to $\approx 277.5 \text{ F cm}^{-3}$ under an ultrahigh scan rate of 1000 mV s^{-1} with a lower charge-transfer resistance and nearly tenfold higher electrochemical active surface area than the 2H-MoS₂ electrode, is reported. Furthermore, 1T'-MoS₂ electrode demonstrates exceptional volumetric desalination capacity of $65.1 \text{ mg}_{\text{NaCl}} \text{ cm}^{-3}$ in CDI experiments. Ex situ X-ray diffraction (XRD) reveal that the cation storage mechanism with the dynamic expansion of 1T'-MoS₂ interlayer to accommodate cations such as Na⁺, K⁺, Ca²⁺, and Mg²⁺, which in turn enhances the capacity. Theoretical analysis unveils that 1T' phase is thermodynamically preferable over 2H phase, the ion hydration and channel confinement also play critical role in enhancing ion adsorption. Overall, this work provides a new method to design compact 2D-layered nanolaminates with high-volumetric performance for CDI desalination.

a significant threat to human health.^[1] To guarantee adequate freshwater supply, desalination has emerged as a promising solution, utilizing abundant seawater and brackish water resources. Conventional desalination techniques, such as reverse osmosis and membrane distillation, are widely employed for treating seawater and brackish water, but they are energy-intensive.^[2-4] Alternatively, capacitive deionization (CDI) offers an energy-efficient and low-carbon footprint approach for removing ions from low-salinity brackish water (concentration $< 1000 \text{ mg L}^{-1}$).^[5-11] Besides, CDI has been utilized to remove heavy metal ions from industrial wastewater and harmful ions in groundwater.^[12,13] The principle of CDI is the electrostatic or electrochemical adsorption of ions from aqueous solution to electrodes, which is similar to electrical double-layer capacitors (EDLC).^[14] Thus, the selection of high performance and space-applicable electrode materials is crucial for the industrialization of CDI technique.^[15,16] In decades, carbon-based materials,^[17-19] including graphene-based material,^[20,21] porous carbon,^[6] as well as derived carbon.^[22] have been extensively investigated owing to their desirable porosity for high ions absorbed surface area.


1. Introduction

Freshwater scarcity is a global challenge, and the additional pollution of freshwater by industrial or agricultural activities poses

T. Ying, Y. Xiong, H. Peng, R. Yang, L. Mei, Z. Zhang, W. Zheng, R. Yan, Y. Zhang, H. Hu, J. Fan, Z. Zeng
Department of Materials Science and Engineering
and State Key Laboratory of Marine Pollution
City University of Hong Kong
83 Tat Chee Avenue, Kowloon, Hong Kong SAR 999077, P. R. China
E-mail: zhiyenzeng@cityu.edu.hk

C. Ma, Y. Chen
Department of Chemistry
Chinese University of Hong Kong
Hong Kong SAR 999077, China

X. Xu
Marine Science and Technology College
Zhejiang Ocean University
Zhoushan, Zhejiang 316022, China

 The ORCID identification number(s) for the author(s) of this article can be found under <https://doi.org/10.1002/adma.202403385>

DOI: 10.1002/adma.202403385

J. Yang
School of Chemical Engineering and Technology
Xi'an Jiaotong University
Xi'an 710049, China

D. Voiry
Institut Européen des Membranes
IEM, UMR 5635
Université Montpellier
ENSCM, CNRS
Montpellier 34000, France

C. Y. Tang
Department of Civil Engineering
University of Hong Kong
Hong Kong SAR 999077, China

Z. Zeng
Shenzhen Research Institute
City University of Hong Kong
Shenzhen 518057, P. R. China

These low density carbon-based electrodes ($0.4\text{--}0.7\text{ g cm}^{-3}$)^[23] deliver a high gravimetric desalination performance but compromising their volumetric one. That makes a challenge to practically employ the CDI technique in certain specific scenarios (e.g., households, islands, or offshore platforms) requiring efficient utilization of space.^[24] In addition, despite the characteristic microporosity of carbon-based materials contributing to large specific surface area, their closed micropores or narrow apertures hamper ion diffusion and thereby slowing down desalination rates.^[25,26] Consequently, achieving compact electrodes with both satisfactory gravimetric and volumetric desalination performance is a challenging yet essential task.^[14,24]

2D materials, e.g., transition metal carbides (MXenes)^[27,28] and transition metal dichalcogenide (TMDs),^[29,30] possess tunable nanochannels, enabling promising electrochemical adsorption of ions and thereby benefiting the desalination performance.^[31] Nonetheless, owing to hydrophilic functional groups attaching to basal plane,^[25,32] MXenes tend to swell in aqueous solution, leading to easily structural disintegration, undesirable CDI performance and poor recyclability.^[17] TMDs, especially MoS₂, are more chemically stable than reported MXenes in seawater and brackish water, making it an optimal candidate for CDI electrode materials.^[33,34] MoS₂ exists in various polymorphs, including 2H, 1T and 1T' phases, distinguished by different intralayer stacking order.^[35–37] These different phases have distinct physical and chemical properties that impact ions electroadsorption performance. Among these polymorphs, the semi-metallic 1T' phase MoS₂ is the thermodynamically preferred and has shown promise in electrochemical energy storage.^[29,38] However, the potential of the 1T'-MoS₂ in CDI system has been underestimated.

In this study, we demonstrate 1T'-MoS₂ nanolaminates with stable nanochannels and compact architecture as superior CDI electrode materials, showing an ideal EDLC behavior and thus achieving high volumetric desalination performance. Our work reveals the nature of ions storage mechanism lies in the dynamically stable nanochannels of 2D-layered materials experimentally and theoretically. Specifically, Ex situ X-ray diffraction (XRD) results demonstrate the adsorption and storage of cations (e.g., Na⁺, K⁺, Ca²⁺, and Mg²⁺) within the 1T'-MoS₂ interlayer leads to the dynamic expansion of nanochannels, which in turn improve the desalination capacity. Theoretical calculations indicate that the phase structure factor governs cations adsorption behavior whereas ion hydration and channel confinement effects further enhance the performance. These findings rationalize the design of compact 1T'-MoS₂ nanolaminates for CDI electrodes and guide the development of other 2D layered materials with high desalination performance.

2. Results and Discussion

2.1. Fabrication and Characterizations

The 1T'-MoS₂ nanosheet aqueous suspension was obtained using our previously reported protocol,^[39–41] i.e., electrochemical lithium intercalation-based exfoliation from bulk 2H-MoS₂ powder (see Experimental Section) (see Figure S1, Supporting Information, for the scanning electron microscope [SEM] image

and XRD pattern of the original MoS₂ powder). The 2H-MoS₂ nanosheet aqueous suspension, as a control, was also prepared via a simple solvent exfoliation method.^[42] Subsequently, 1T'-MoS₂ and 2H-MoS₂ electrode were further fabricated by restacking the exfoliated nanosheets onto a flexible current collector via vacuum filtration and dehydration (Figure 1a). Note that the zeta potential value of 1T'-MoS₂ nanosheets is negative (-53.2 mV , Figure S2, Supporting Information), indicating the presence of negative charges.

Transmission electron microscopy (TEM) image (Figure 1b) shows the flake-like morphology of the exfoliated 1T'-MoS₂ nanosheets. The selected area electron diffraction (SAED) pattern exhibits a typical diffraction pattern of hexagonal symmetry (inset of Figure 1b). Atomic force microscopy (AFM) analysis (Figure S3, Supporting Information) confirms the ultra-thin attribute of the exfoliated 1T'-MoS₂ nanosheets with thickness ranging from 1.1 to 1.8 nm. Scanning transmission electron microscopy (STEM) images (Figure 1c; Figures S4–S6, Supporting Information) display a distinctive Mo atomic structures of zigzag chains with shortest Mo-Mo distance of 2.79 Å (Figure S5, Supporting Information) of the lithium intercalation-based exfoliated MoS₂ nanosheets, suggesting their distorted octahedral (1T') phase.^[35] (Figure 1d), which was further confirmed by the corresponding fast Fourier transform (FFT) pattern (inset of Figure 1c).

The prepared 1T'-MoS₂ electrode exhibits excellent flexibility (Figure 1f). Cross-sectional SEM image (Figure 1g) reveals the typical lamellar and compact architecture of 1T'-MoS₂ electrode with a thickness of 1000 nm. Varying thickness (i.e., 300, 2000, 3000, and 4300 nm) of 1T'-MoS₂ electrodes can be prepared by adjusting the volume of filtrated solution (Figure S7, Supporting Information). The surface of the prepared electrode is notably flat, as confirmed by the average surface roughness value of 37 nm (Figure S8, Supporting Information). High-resolution TEM (HR-TEM) image demonstrates the interlayer spacing of 0.62 nm from horizontal MoS₂ nanolaminates (Figure 1h), which is close to the spacing observed in bulk MoS₂. Characteristic peaks of 2H-MoS₂ dispersion located at 409, 478, 615, and 673 nm, can be clearly observed in the UV-vis absorption spectra as denoted by the dashed lines (Figure S9, Supporting Information). Raman peaks of the 2H-MoS₂ electrode (Figure 2a), located at 377.4 and 402.7 cm⁻¹ are two characteristic modes,^[41] corresponding to E_{2g} (in-plane vibration) and A_{1g} (out-of-plane vibration). Conversely, the 1T'-MoS₂ electrode exhibits additional modes such as J_1 (148.3 cm⁻¹), J_2 (221.2 cm⁻¹), J_3 (326.1 cm⁻¹), and E_{1g} (286.1 cm⁻¹), along with the absence of E_{2g} modes.^[43] In the X-ray diffraction (XRD) patterns (Figure 2b), the peak of the (002) plane for the dehydrated 1T'-MoS₂ electrode is located at $\approx 14^\circ$, validating the quasi-perfect restacking of the pristine nanosheets, resembling that of bulk MoS₂.^[29,44] The average (002) spacing of the dehydrated 1T'-MoS₂ electrode is 0.63 nm, consistent with HR-TEM results (Figure 1h). Due to the hydrophilic nature of 1T'-MoS₂ (Figure S10, Supporting Information), the peak of hydrated 1T'-MoS₂ electrode shifted to a lower angle of 8.5°, corresponding to spacing of 1.0 nm (Figure 2b). In contrast, the (002) plane of 2H-MoS₂ electrode closely aligns with the position of bulk MoS₂ powder (14.3°, Figure S1, Supporting Information). X-ray photoelectron spectroscopy (XPS) was employed to examine the chemical states of the two electrodes from the Mo 3d (Figure 2c,d) and S

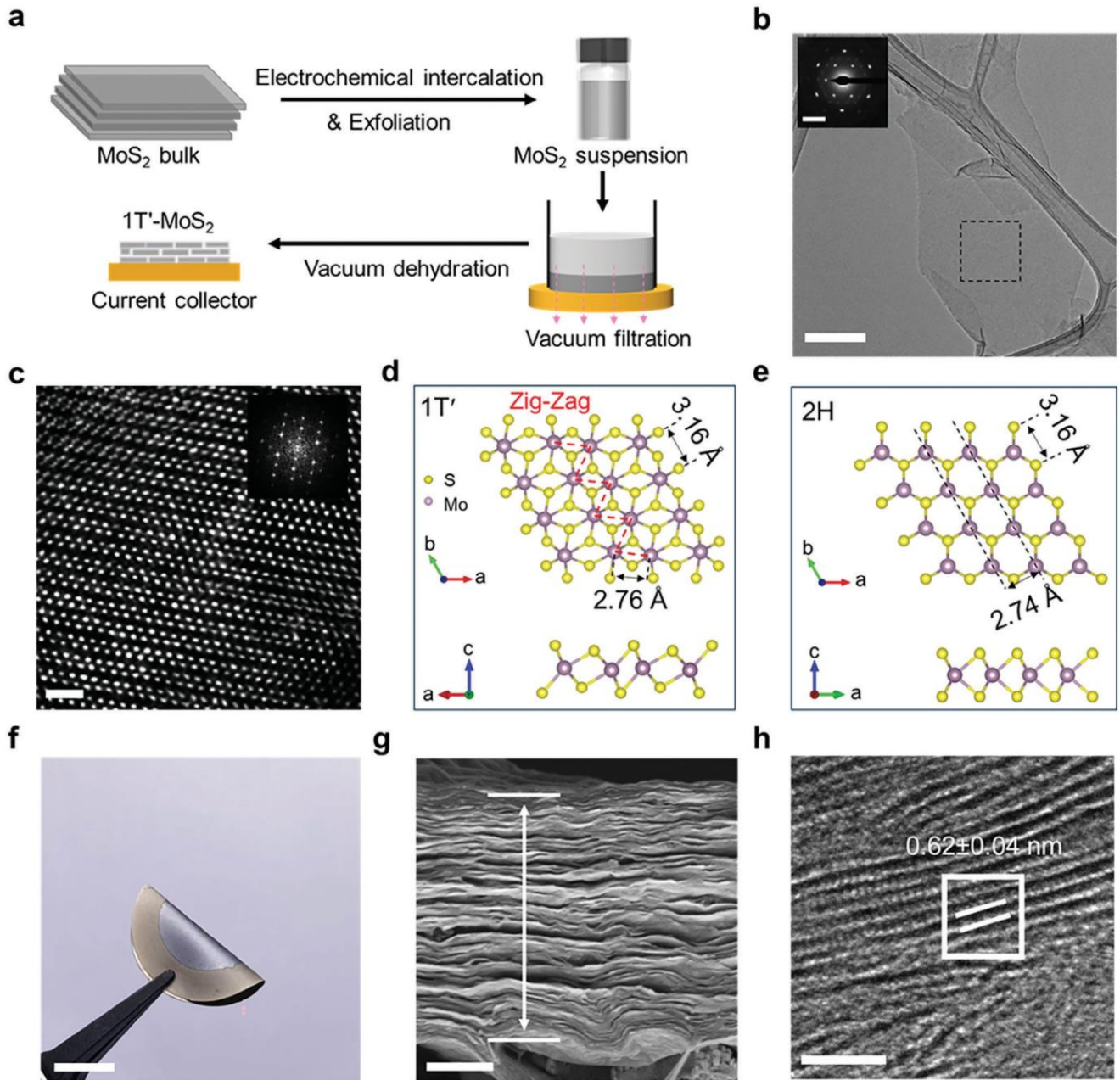


Figure 1. Fabrication and electron microscopy characterizations of 1T'-MoS₂ nanosheets and electrode. a) Schematic illustration of the fabrication of 1T'-MoS₂ nanosheets and electrode via electrochemical lithium intercalation-based exfoliation method and vacuum filtration method (onto Au-coated PVDF substrate). b) TEM image of the exfoliated MoS₂ nanosheets. Scale bar, 200 nm. Inset: SAED pattern of the area denoted by black dashed rectangular box. Scale bar, 5 1/nm. c) HAADF-STEM image of the exfoliated 1T'-MoS₂ nanosheets. Scale bar, 1 nm. Inset: the corresponding fast Fourier transform (FFT) pattern. Schematic illustrations of the atomic structures of (d) 1T'-MoS₂ and (e) 2H-MoS₂, respectively. The red dashed lines in (d) demonstrate the zig-zag chain of Mo atoms in 1T'-MoS₂. f) Photo of a 1T'-MoS₂ membrane fabricated by vacuum filtration with good flexibility. Scale bar: 1 cm. g) Cross-section SEM view of 1T'-MoS₂ electrode prepared by vacuum filtration, showing compact lamellar architecture. Scale bar: 300 nm. h) Cross-sectional TEM observations of horizontal 1T'-MoS₂ laminates with the separation of ≈ 0.62 nm. Scale bar: 5 nm.

2p (Figure 2e,f) regions. For the 2H-MoS₂ electrode, Figure 2c presents deconvolution of the Mo 3d regions (227–234 eV) of two distinct peaks, indicating the exclusive presence of the 2H phase. This is further confirmed by the presence of only two characteristic peaks in the S 2p spectrum (160–165 eV) (Figure 2e). In contrast, 1T'-MoS₂ electrode (Figure 2d) exhibits character-

istic peaks of the 1T' phase, which shifted to lower values by ≈ 0.8 eV compared with the 2H phase.^[43] Based on the XPS data from the Mo 3d region (Table S1, Supporting Information), the percentage of 1T' phase can reach up to 73%. Figure 2f demonstrates that the exfoliated MoS₂ nanosheets display two doublets in the S 2p region, consistent with the presence of both 1T' and

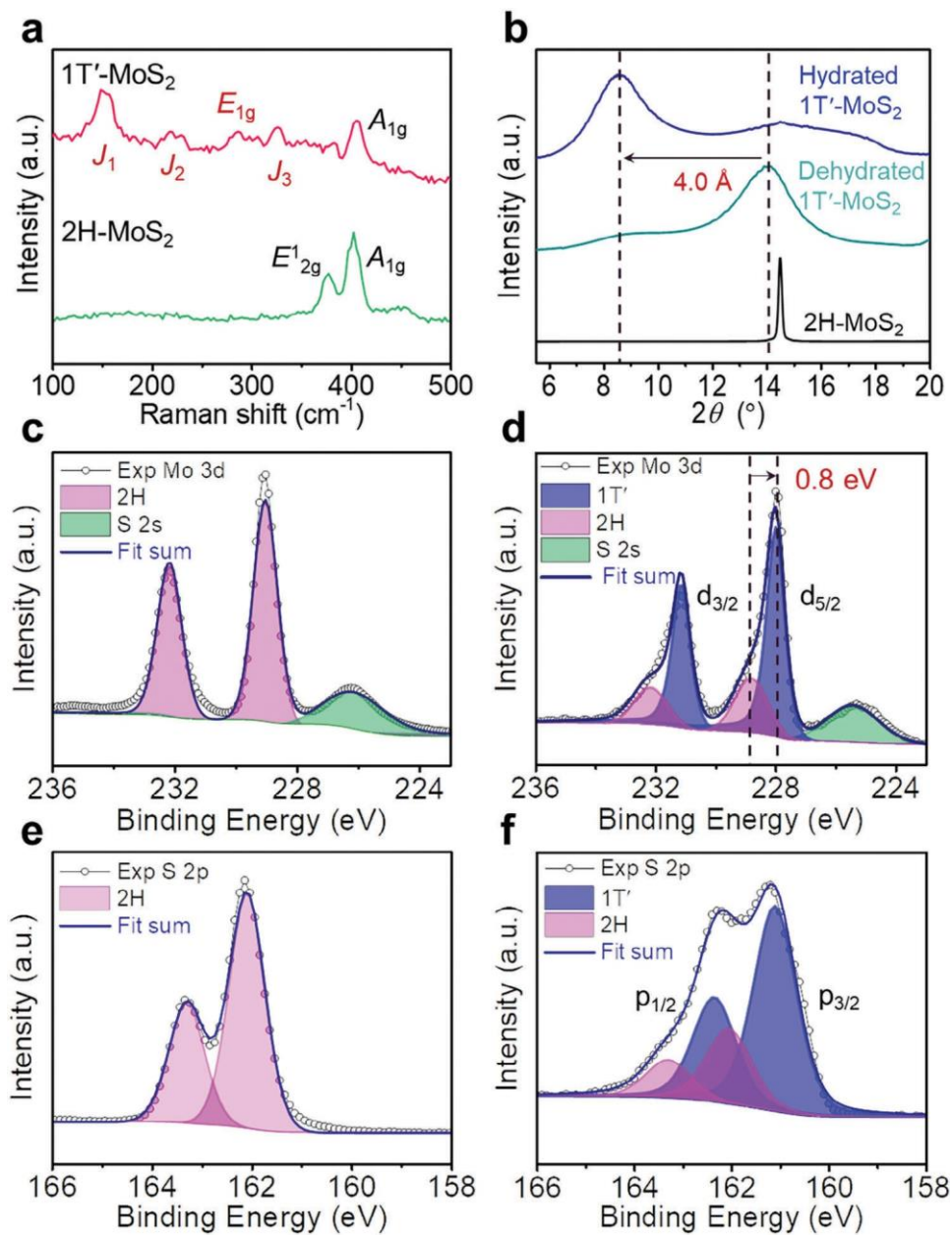


Figure 2. Raman, XRD, and XPS characterization of 1T' and 2H-MoS₂ electrodes. a) Raman spectroscopy. The 1T'-MoS₂ electrode shows distinctive Raman modes of J_1 , J_2 , J_3 and E_{1g} . b) XRD patterns of the hydrated and dehydrated 1T'-MoS₂ and 2H-MoS₂ electrodes. Hydration gives rise to the enlarged interlayer spacing of 1T'-MoS₂ electrode with ≈ 4.0 Å. XPS spectra of 2H-MoS₂ electrode (c, Mo 3d and e, S 2p) and 1T'-MoS₂ electrode (d, Mo 3d, f, S 2p). The characteristic peaks of the 1T' phase shifted to lower value by ≈ 0.8 eV compared with the 2H phase. a.u., arbitrary units.

2H phases in exfoliated MoS₂. According to characterizations above, we finally confirmed the 1T'-MoS₂ nanolaminates with stable nanochannels and compact architecture were successfully fabricated.

2.2. Electrochemical Properties

To differentiate the effect of polymorphs on CDI desalination performance, the electrochemical properties of the 2H and 1T'-

MoS₂ electrodes, were evaluated by cyclic voltammetry (CV) using a conventional three-electrode set-up at room temperature in a 1 M KCl electrolyte, where the Ag/AgCl electrode and Pt plate served as reference and counter electrodes, respectively. The near-rectangular and symmetric shape of 1T'-MoS₂ electrode indicates typical EDLC behavior, achieving a capacitance of 95 F g^{-1} at 50 mV s^{-1} , in contrast to the less favorable shape observed for 2H-MoS₂ electrode with 35 F g^{-1} (Figure 3a). As scan rates increase from 10 to 1000 mV s^{-1} , the well-preserved EDLC behavior of the 1T'-MoS₂ electrode demonstrates its

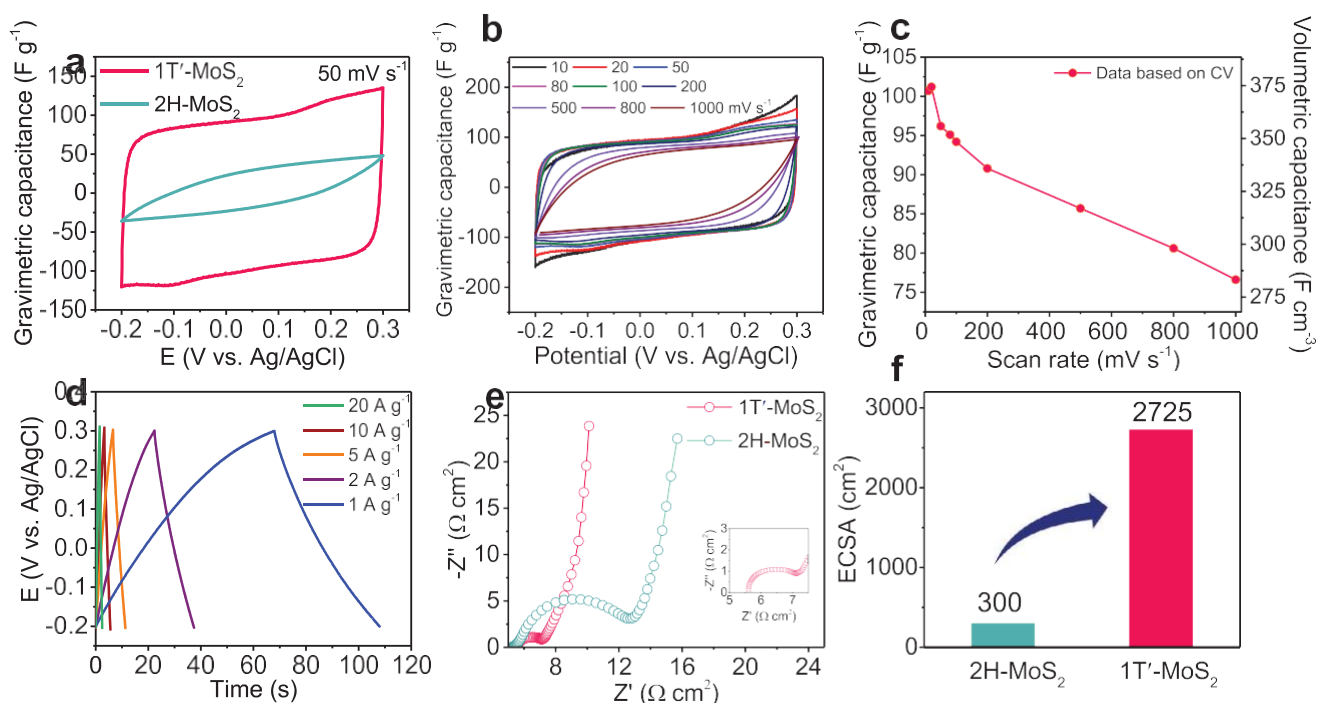


Figure 3. Electrochemical properties of the 1T'-MoS₂ electrode in 1 M KCl electrolyte. a) Cyclic voltammograms of 2H and 1T'-MoS₂ electrodes with the scan rate of 50 mV s⁻¹. The 1T'-MoS₂ electrode shows the near-rectangular and symmetric curves with EDLC behavior compared to the less favorable shape of 2H-MoS₂ electrode. b) Cyclic voltammograms of 1T'-MoS₂ electrode over scan rates from 10 to 1000 mV s⁻¹, showing the excellent and stable performance of 1T'-MoS₂ electrode even at an ultrahigh scan rate. c) Gravimetric capacitance and volumetric capacitance of 1T'-MoS₂ electrode decreased with increased scan rates. d) Galvanostatic charge-discharge (GCD) data of 1T'-MoS₂ electrode collected from 1 to 20 A g⁻¹. e) Electrochemical Impedance Spectroscopy (EIS) data for the 1T'-MoS₂ and 2H-MoS₂ electrodes. Inset: the zoom-in data of EIS result for 1T'-MoS₂ electrode. f) Calculated electrochemical active surface area (ECSA) for 2H and 1T'-MoS₂ electrodes: demonstrating nearly tenfold larger ECSA value for 1T'-MoS₂ compared with 2H-MoS₂ electrode.

robust performance under ultrahigh charge and discharge rate (Figure 3b) while the capacitance of 2H-MoS₂ electrode deteriorates at 100 mV s⁻¹ (Figure S11, Supporting Information). Specifically, the 1T'-MoS₂ electrode delivers a capacitance of 101 F g⁻¹ (373 F cm⁻³) at 20 mV s⁻¹ and slightly decreases with increased scan rates from 50, 80, 100, 200, 500, 800 to 1000 mV s⁻¹, but remains at 75 F g⁻¹ (277.5 F cm⁻³) even under ultrahigh scan rate of 1000 mV s⁻¹, highlighting its excellent rate performance (Figure 3c). Figure 3d presents the galvanostatic data collected at different current densities (1, 2, 5, 10, and 20 A g⁻¹) with corresponding charging and discharging time ranging from 107, 37, 11, 6, 2 s, respectively. The triangular and symmetric shapes also support the EDLC effect of 1T'-MoS₂ electrode. The electrochemical impedance spectroscopy (EIS) results provide a powerful platform to analyze the electron transfer properties. Notably, the charge-transfer resistance (R_{ct}) between the electrode and interface is closely related to the diameter of the quasi-semicircle. As shown in Figure 3e, the 1T'-MoS₂ electrode exhibits a lower R_{ct} of 2.5 Ω cm² compared with the 7 Ω cm² for 2H-MoS₂ electrode. The analysis of the electrochemical active surface area (ECSA) (Figure 3f; Figure S12, Supporting Information) reveals that the ECSA value of 1T'-MoS₂ (2725 cm²_{ECSA}) is nearly tenfold greater than that of 2H-MoS₂ (300 cm²_{ECSA}), demonstrating the superiority of 1T'-MoS₂ in electrochemical active surface area.

2.3. Capacitive Desalination Performances

To further investigate the impact of polymorphs on electro-sorption of ions, we conducted evaluations of the CDI desalination performance using NaCl solution (low salinity, 500 mg L⁻¹) in constant-voltage single-batch measurements. Figure 4a presents a schematic illustration of the CDI working mechanism. Specifically, two symmetric electrodes were immersed in aqueous solutions with a conductivity meter inserted in the middle of the cell to monitor conductivity (Figures S13 and S14, Supporting Information). The salt adsorption capacity measured in gravimetric adsorption capacity (GAC, Γ_g , mg_{NaCl} g⁻¹) is an important indicator reflecting the maximum salt adsorption capability. As shown in Figure 4b, when a bias voltage of 0.5 V was applied across the two electrodes, the GAC of the 1T'-MoS₂ electrode increases to 13 mg_{NaCl} g⁻¹ within the first 200 s and gradually approaches a steady capacity of 17.6 mg_{NaCl} g⁻¹ in the following 1000 s. In contrast, the GAC of the 2H-MoS₂ electrode quickly reaches a plateau of 5 mg_{NaCl} g⁻¹ within the first 100 s. The increased GAC curves of the electrodes agreed well with the current density profiles (Figure S15, Supporting Information).^[6] Figure 4c shows the average salt adsorption rate (ASAR) in the form of Kim-Yoon Ragone diagram.^[45] The ASAR of 2H-MoS₂ electrode quickly drop below 1 mg_{NaCl} g⁻¹ min⁻¹ when GAC exceeds 6 mg_{NaCl} g⁻¹ while 1T'-MoS₂ electrode can

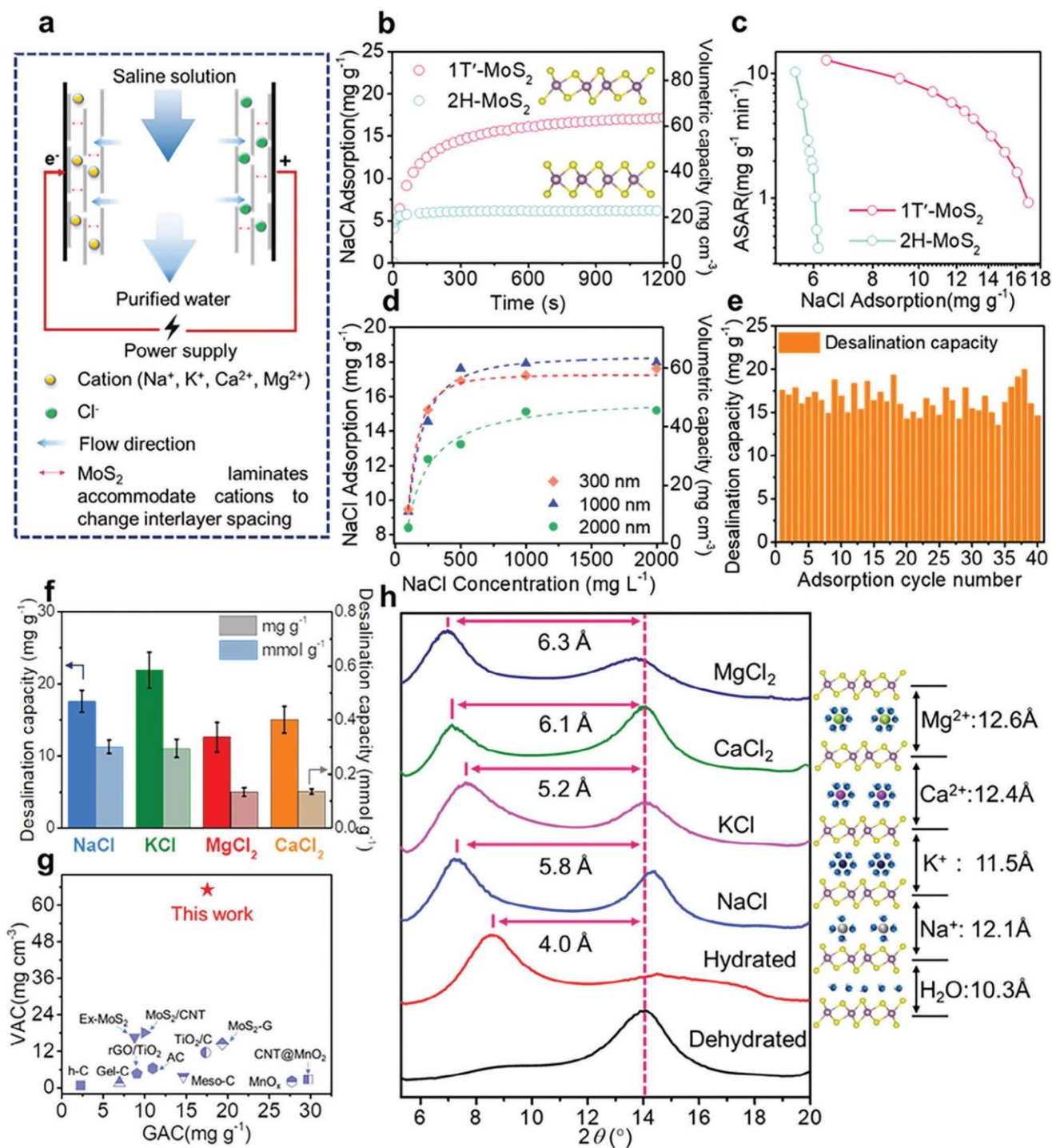


Figure 4. Capacitive desalination performances and mechanism study. a) Schematic illustration of CDI working mechanism. b) Typical time-resolved gravimetric adsorption capacities (GAC) profiles of 1T'-MoS₂ and 2H-MoS₂ electrodes in 500 mg L⁻¹ NaCl solution. c) Kim-Yoon CDI Ragone diagram of 1T'-MoS₂ in contrast with 2H-MoS₂ electrode. d) GAC of 1T'-MoS₂ electrode with respect to different initial concentration of NaCl solution. Dashed lines represent the Langmuir fitting of the adsorption isotherm data. Error bars are omitted for clarity. e) Repeated adsorption-desorption cycles for NaCl desalination of the 1T'-MoS₂ electrode. f) GAC and molar desalination capacities of 1T'-MoS₂ electrode for NaCl, KCl, MgCl₂, and CaCl₂ deionization. Error bars represent s. d. of three independent measurements. g) Comparison of volumetric adsorption capacities (VAC) versus GAC of reported state-of-the-art materials and MoS₂ laminates of this work. The detailed data of literature are listed in Table S2 (Supporting Information). h) Ex situ XRD patterns of restacked 1T' phase MoS₂ electrode immersed in different saline solutions. The enlarged interlayer spacing of electrodes are denoted on the right for clarification with respective cations and water molecule, showing the dynamic accommodation effect of MoS₂ nanochannels.

maintain the ASAR over $1 \text{ mg}_{\text{NaCl}} \text{ g}^{-1} \text{ min}^{-1}$ until the GAC approaches $16 \text{ mg}_{\text{NaCl}} \text{ g}^{-1}$, further demonstrating the rapid desalination performance of our 1T'-MoS₂ electrode.

We also investigated the effect of electrode thickness on the adsorption capacity with different initial saline concentrations. As shown in Figure 4d, all the GAC of electrodes with different thicknesses (300, 1000, 2000, 3000, and 4300 nm) follow the Langmuir adsorption isotherm representing the relationship between the quantity of adsorbed salt and the NaCl initial concentration (dashed lines). We found that the thickness of the electrodes influenced the adsorbed quantities. For instance, when the initial NaCl concentration is 500 mg L^{-1} , the NaCl adsorption quantity for electrodes with thicknesses of 300, 1000, 2000 nm is 16.9, 17.6, 13.2 $\text{mg}_{\text{NaCl}} \text{ g}^{-1}$, respectively. Obviously, too thick nanochannels may introduce resistance in cation transport, thereby reducing the overall adsorption capacity. When increasing the NaCl initial concentration from 1000 to 2000 mg L^{-1} , the NaCl adsorption reaches saturation, and the GAC of 300, 1000, 2000 nm-thickness electrode remains at 17.1, 17.6, 15.4 $\text{mg}_{\text{NaCl}} \text{ g}^{-1}$, respectively, indicating the capacity is related with the thickness. Figure S16 (Supporting Information) shows the XPS depth profile of the Na element after CDI measurements, exhibiting uniformly distributed adsorbed Na⁺ within the MoS₂ layers. The depth ranges from 30 to 90 nm, corresponding to ≈ 48 –145 layers of MoS₂.

For long-term stability assessment, the 1T'-MoS₂ electrode was subjected to 40 charge-discharge repeats with recycled CDI operation, rinsing, and re-hydration. After 40 cycles, the average GAC of 1T'-MoS₂ remained at $\approx 14.61 \text{ mg}_{\text{NaCl}} \text{ g}^{-1}$ (83%), indicating that CDI electrodes exhibited no substantial loss of desalination capacity after repeated charge-discharge cycles (Figure 4e). Post characterization also showed structural integrity after the CDI experiment, confirming the physical stability of our 1T'-MoS₂ electrode (Figures S17 and S18, Supporting Information). Furthermore, we evaluated the versatile performance of the 1T'-MoS₂ electrode in different saline solutions. As depicted in Figure 4f, the gravimetric desalination capacity for K⁺ was the highest (22.0 mg g^{-1}), followed by Na⁺ (17.6 mg g^{-1}), Ca²⁺ (15.1 mg g^{-1}), and Mg²⁺ (12.6 mg g^{-1}). The molar desalination capacity of Na⁺ (0.301 mmol g^{-1}) and K⁺ (0.295 mmol g^{-1}) was similar, while Ca²⁺ (0.136 mmol g^{-1}) and Mg²⁺ (0.134 mmol g^{-1}) were approximately half as much. This result suggests that the quantity of carrying charges (e.g., K⁺/Na⁺ with one charge and Ca²⁺/Mg²⁺ with two charges) may determine the maximum electro-adsorption capacity. Based on the results, the 1T'-MoS₂ electrode was versatile and capable of removing common cations, i.e., K⁺, Na⁺, Mg²⁺, and Ca²⁺ from low-salinity brackish water.

The calculation of volumetric adsorption capacity (VAC, Γ_V , $\text{mg}_{\text{NaCl}} \text{ cm}^{-3}$), is analogous to the volumetric capacitance (C_v , F cm^{-3}) which is determined by the product of gravimetric capacitance (C_g , F g^{-1}) and the density of electrodes (ρ , g cm^{-3}).^[46] Therefore, the volumetric desalination capacity of our compact 1T'-MoS₂ electrode can be expressed as,^[29]

$$\Gamma_V = \Gamma_g \times \rho \quad (1)$$

here, the density of the hydrated electrode (ρ) was measured to be $\approx 3.7 \text{ g cm}^{-3}$ owing to the densely compact architecture, which is lower than that of reported bulk MoS₂ powder^[44] but higher than carbon-based materials ones.^[23] To provide an overview of the

performance compared with state-of-the-art electrodes, we summarized the VAC and GAC of 1T'-MoS₂ electrode in Figure 4g, with data from previous literature on carbon-based and 2D-based materials (Table S2, Supporting Information).^[47] The red star representing our EDLC-type 1T'-MoS₂ electrode demonstrates superior VAC performance ($65.1 \text{ mg}_{\text{NaCl}} \text{ cm}^{-3}$), and its GAC performance ($17.6 \text{ mg}_{\text{NaCl}} \text{ g}^{-1}$) is excellent when compared with state-of-the-art materials. Notably, our EDLC-type 1T'-MoS₂ electrodes exhibited improved VAC performance based on the utilization of horizontal nanochannels of compact architecture.

2.4. Cation Storage Mechanism

Ex situ XRD measurements were performed on CDI electrodes intercalated with different electrolytes including deionized water and 0.5 M saline solutions (NaCl, KCl, CaCl₂ and MgCl₂) to investigate the cation storage mechanism in 1T'-MoS₂ electrodes (Figure 4h). As intercalation proceeds, the intensity of the (002) peak at 14.1° from restacked 1T'-MoS₂ decreases slightly, and the intensity of new peak appears at lower angle, indicating that interlayer expansion between consecutive S-Mo-S layers caused by intercalation of cations or water molecules. Notably, the extent of interlayer spacing expansion strongly depends on the types of intercalants. Expansions of the spacing between consecutive S-Mo-S layers are 4.0, 5.8, 5.2, 6.1, and 6.3 Å for pure water, Na⁺, K⁺, Ca²⁺, and Mg²⁺, respectively. This finding is also related to the fact that hydrated diameter of K⁺ (6.62 Å) is smaller than that of Na⁺ (7.16 Å), Ca²⁺ (8.24 Å), and Mg²⁺ (8.56 Å). The dynamic expansion of the interlayer spacings of the 1T'-MoS₂ suggests that the electrodes are capable of accommodating cations dynamically,^[38] which in turn, is beneficial to the enhancement of desalination capacity.

To further elucidate the cation storage mechanism during CDI process, we distinguished the crucial roles of structure factor, ion hydration, and confinement effects in desalination performance using density functional theory (DFT) calculations and ab initio Molecular Dynamics (AIMD) simulations. The adsorption energy (E_{ad}) for a single K⁺ on different initial sites of the 1T' and 2H-MoS₂ surfaces were first calculated and summarized (Figure S19, Supporting Information). We selected the configuration with the most favorable adsorption site (most negative values of E_{ad}) and presented the structures, i.e., Mo₁ site on 1T'-MoS₂ (Mo₁-1T'), Mo site on 2H-MoS₂ (Mo-2H), and respective 2D channels were constructed (see the top and side view of atomic structures in Figure 5a; Figure S20, Supporting Information). As shown in Figure 5b, the E_{ad} of Mo₁-1T' (-2.38 eV) is significantly lower than that of Mo-2H (-0.73 eV) in the vacuum state, suggesting the 1T' phase exhibits enhanced adsorption capabilities against the 2H phase. This is because the 1T' phase shows a higher degree of asymmetry, resulting in an active surface with increased adsorption sites, and thus a more conducive adsorption structure compared with the 2H phase. Upon the introduction of a K⁺ within the MoS₂ channel, the E_{ad} for Mo₁-1T' (-2.79 eV) and Mo-2H (-1.26 eV) decrease slightly, indicating that channel confinement effect can facilitate the ion adsorption. Surprisingly, when accounting for the solvent effect, the E_{ad} of K⁺ nearly doubles (-4.47 eV for 1T'-MoS₂ while -2.93 eV for 2H-MoS₂), indicating that the solvation enhanced the interaction between the

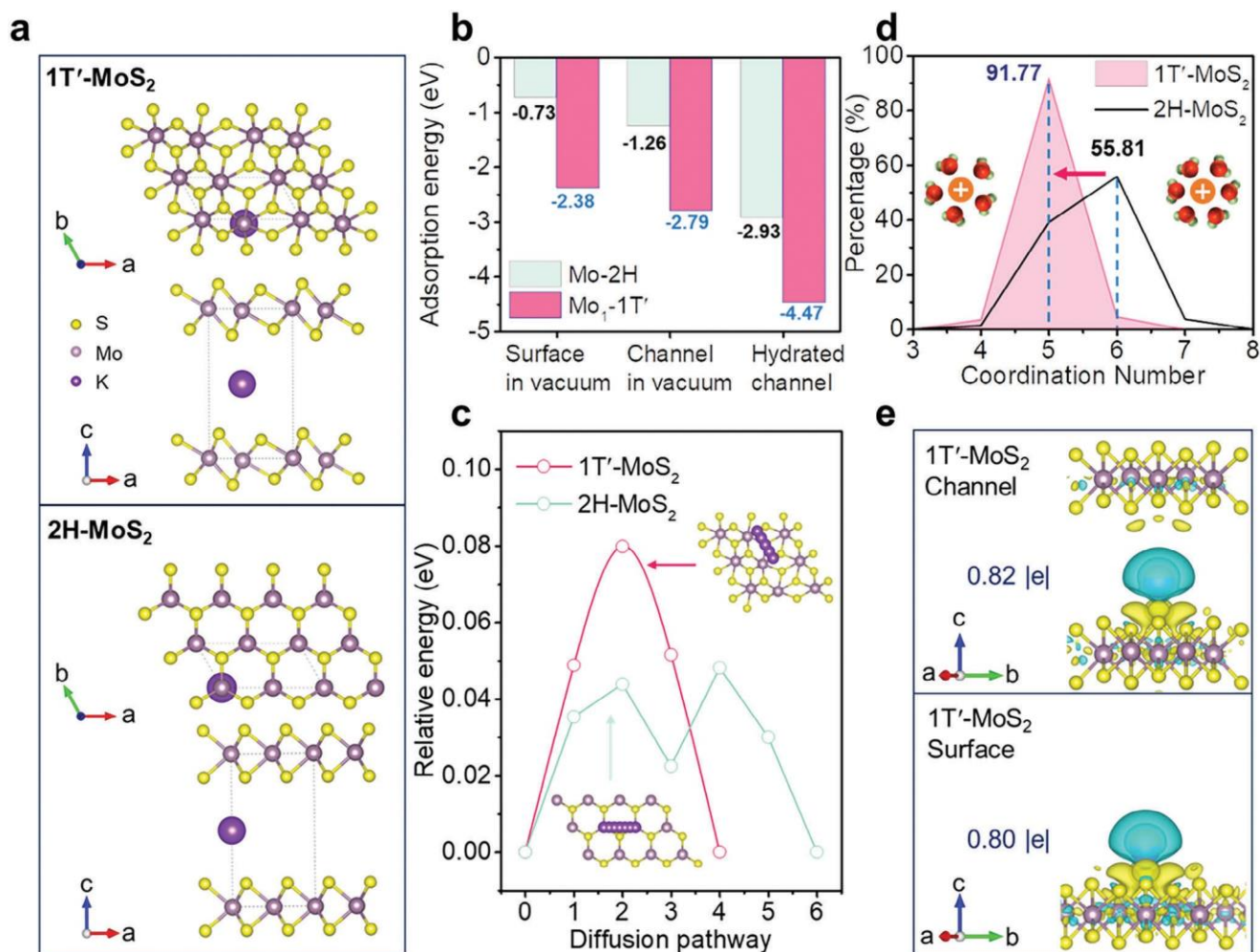


Figure 5. DFT calculations and AIMD simulations of the interaction between K^+ and MoS_2 . a) Schematic illustrations of atomic structures of preferred K^+ adsorbed position on the basal plane of $1T'$ - MoS_2 , 2H- MoS_2 (denoted as Mo_1-1T' , $Mo-2H$) and in the respective 2D channels. b) Interaction energy of K^+MoS_2 with the conditions of MoS_2 surface in vacuum, MoS_2 channels in vacuum and hydrated MoS_2 channels. We selected the most stable initial sites for comparison. c) Migration energies of K^+ when diffusing via possible pathway on the surface. Inset: possible diffusion pathway for 2H and $1T'$ - MoS_2 surface. d) Probability partition of the cation's coordination number with water in the 2H and $1T'$ - MoS_2 channels. e) The charge density difference of K^+ in the channel and surface of $1T'$ - MoS_2 , and the corresponding charge transfer from metal to the channel. The isosurface level is set as $0.001 e \text{ \AA}^{-3}$.

K^+ and the MoS_2 channel. These results highlight the important factors of both confinement and hydration effects contributing to exceptional adsorption performance. Similar trends were found for other adsorption sites as the E_{ad} of 2H- MoS_2 were smaller than that of $1T'$ - MoS_2 at all possible adsorption sites (see Table S3, Supporting Information).

To investigate the diffusion behavior of ions in the channel of $1T'$ and 2H- MoS_2 , we analyzed the diffusion energy barriers based on the climbing image nudged elastic band (CI-NEB) method. Figure 5c displays a higher diffusion barrier for the $1T'$ - MoS_2 channel (0.079 eV) compared with 2H- MoS_2 channel (0.048 eV), suggesting a more challenging migration path in the $1T'$ channel. While easy migration may facilitate ion transport, it may hamper effective ion adsorption. For the study of ions hydration effect, the AIMD simulations were performed to analyze the hydration structure of solvated ions in the channel of MoS_2

with different phases (Figure S21 and Video S1, Supporting Information, for $1T'$ - MoS_2 , Figure S22 and Video S2, Supporting Information, for 2H- MoS_2). We note that coordination number (CN) distribution of water molecules varies from the $1T'$ to 2H phase. For a K^+ in the $1T'$ channel, the majority of CN is predominantly 5 (91.77%), while the CN of the 2H phase is 6 (55.81%) (Figure 5d). The decreased CN of the hydration shell resulted in partial exposure of the K^+ core, allowing direct contact with the $1T'$ - MoS_2 layer and thus enhancing the interaction between the metal ion and the layered materials.^[48] Next, the Bader charge density analysis suggests that more charge transfers from K^+ to the $1T'$ channel (0.82 |e|) than the $1T'$ surface (0.80 |e|), as demonstrated in Figure 5e and Figure S23 (Supporting Information). Such charge transfer indicates the increased ion- MoS_2 interaction when ions exist in the limited nanochannels. Overall, our theoretical calculations demonstrate that the $1T'$ - MoS_2 structure

governs K^+ adsorption behavior by increasing the interaction of K ions to their adsorption sites in the S-Mo-S channel, thereby providing a superior desalination performance in CDI applications.

3. Conclusion

In summary, our study has demonstrated that the compact 1T'-MoS₂ electrode, devoid of binders, exhibits ideal EDLC behavior at 1000 mV s⁻¹ and displays high volumetric desalination per-

formance (65.1 mg_{NaCl} cm⁻³) in CDI configurations. This excep-

tional performance can be attributed to the metastable 1T' phase structure of MoS₂, compact laminated architecture featuring intrinsic nanochannels, bringing about its unique characteristics of low charge-transfer resistance and high electrochemical active surface area to accommodate various cations. The experimental analysis and theoretical calculations have revealed that compared with 2H phase, cations prefer adsorbed on the Mo sites of 1T'-MoS₂ and in the channels of the 1T' phase. Moreover, ion hydration and channel confinement effects help to enhance ion adsorption performance. Following these results, we believe that our EDLC-type 1T'-MoS₂ electrode can be favorable state-of-the-art nanolaminated materials for integration into miniaturized CDI desalination system.

4. Experimental Section

Exfoliation of MoS₂ Bulk Powder: The MoS₂ nanosheets obtained by electrochemical lithium exfoliation-based intercalation are on ground of previous reported protocol.^[35-37] Typically, the slurry containing MoS₂ powder, carbon black, and PVDF (8:1:1) mixed with NMP was fabricated into an electrode plate. The plate acted as a cathode was assembled into a testing coin cell and then discharged to perform the lithium intercalation. After that, the lithium-intercalated cathode (Li_xMoS₂) was separated from the dissembled cell when the discharging process finished. Finally, the MoS₂ nanosheets were obtained via sonication of the electrodes in DI water for 1 h, during which the generated gas (H₂) bubbles accelerated the exfoliation of the bulk MoS₂. The centrifugation and re-dispersion process (repeated at least three times) is indispensable to remove the multiple layers of MoS₂ nanosheets. Thus, single layer of 1T'-MoS₂ nanosheets were successfully synthesized.

Preparation of MoS₂ Electrodes: The 1T'-MoS₂ electrode were fabricated through vacuum filtration reported previously.^[34] Briefly, porous polymeric supports were sputtering coated with Au thin layer first. Of note, polymeric supports are typically made of nylon or PVDF with 220 nm pore sizes. Then, the suspension of exfoliated 1T'-MoS₂ nanosheets was filtered over flexible, conductive polymeric supports. The density of the 1T'-MoS₂ hydrated electrodes were measured to be ≈3.7 g cm⁻³. The 2H-MoS₂ electrode was fabricated by filtration suspension of solvent exfoliation of bulk materials as previously reported.^[42]

Electrochemical Measurements and CDI Performance: The electrochemical performance was measured in a three-electrode system at room temperature with variation less than 0.3 °C. A Pt plate, an electrode (Ag/AgCl), 1 M KCl aqueous solution were used as the counter electrode, the reference electrode, and the electrolyte, respectively. Cyclic voltammetry (CV), galvanostatic charge-discharge (GCD), electrochemical impedance spectroscopy (EIS), and cycling stability studies were carried out on an Ivium potentiostat system. CV scans were conducted at scan rates ranging from 10 to 1000 mV s⁻¹. Galvanostatic cycling scans were performed at current densities ranging from 1 to 20 A g⁻¹. The EIS was performed with frequencies ranging from 100 kHz to 0.01 Hz and a sinusoidal voltage of 5 mV. The batch-mode CDI experiment was carried out in a custom-made cell filled with 20 mL saline solution at room temperature with the variation less than 0.3 °C. The symmetrical electrode

system was assembled using as-prepared electrodes, then immersed in the saline solution to serve as working and counter electrodes. A conductivity meter (SevenMulti, METTLER TOLEDO) was used to monitor the conductivity of the NaCl solution in real time curves (Figure S13, Supporting Information). The conductivity of NaCl solution is linear relative to the concentration, as depicted in calibration curves (Figure S14, Supporting Information). The desalination potential was set at a relatively low constant voltage (0.5 V) to avoid hydrogen evolution reaction. Before measurements, the two electrodes were submerged in the solution without an external bias to minimize the effects of initial physisorption.

Computational Method: All calculations were carried out by the Vienna ab initio simulation package (VASP) based on density functional

theory (DFT).^[49-51] The generalized gradient approximation (GGA) of the Perdew-Burke-Ernzerhof (PBE) exchange correlation functional was used to describe the exchange-correlation interactions.^[52-54] The plane-wave cutoff energy was set to 500 eV. The convergence standard for the total energy and ionic force were set to 10⁻⁵ eV and 0.02 eV Å⁻¹, respectively. The DFT-D3 method was employed to consider the influence of van der Waals (vdWs) interaction. To study the influence of water on ion adsorption on the MoS₂ channel, the implicit solvation (VASPsol) correction was applied.^[55,56] The dielectric constant of water was set to ε_b = 78.4. In addition, the ab initio molecular dynamics (AIMD) simulations were performed to understand the transport properties and hydration structure of solvated ions in the MoS₂ channel. The simulation parameters were set to 300 K in a total of 30 ps with the time step of 1 fs.

Supporting Information

Supporting Information is available from the Wiley Online Library or from the author.

Acknowledgements

Z.Y.Z. thanks the Young Collaborative Research Grant [Project No. C1003-23Y] and General Research Fund (GRF) [Project No. CityU11308923] support from the Research Grants Council of the Hong Kong Special Administrative Region, China, the Basic Research Project [No. JCYJ20210324134012034] from Shenzhen Science and Technology Innovation Committee in Shenzhen, China, the Applied Research Grant of City University of Hong Kong (project no of 9667247) and Chow Sang Sang Group Research Fund of City University of Hong Kong (project no of 9229123). Z.Y. Z. also thanks the funding supported by the Seed Collaborative Research Fund Scheme of State Key Laboratory of Marine Pollution which receives regular research funding from Innovation and Technology Commission (ITC) of the Hong Kong SAR Government. However, any opinions, findings, conclusions or recommendations expressed in this publication do not reflect the views of the Hong Kong SAR Government or the ITC. J. Fan thanks the Hong Kong Research Grant Council Collaborative Research Fund [No. C1002-21G]. This research made use of the computing resources of the X-GPU cluster supported by the Hong Kong Research Grant Council Collaborative Research Fund [No. C6021-19EF].

Conflict of Interest

The authors declare no conflict of interest.

Author Contributions

Z.Y.Z. conceived the research direction and guided the project. T.Y., Y.X., and H.P. contributed equally to this work. T.Y. and H.P. prepared the electrode samples and completed most of the experiments and characterizations. L.M., W.Z., R. Y., Y.Z., and H.H. helped with XPS, XRD analysis. Y.X. and J.F. carried out theoretical calculations and analysis. Z.Z. performed

STEM characterizations and analyzed the data. C.M. and Y.C. helped with the TEM characterizations. X.X., J.Y., D.V., and C.T. provide helpful discussion into the experiment and the manuscript. T.Y., H.P., Y.X., R.J.Y., J.F., and Z.Y.Z. co-wrote the manuscript. All authors contributed to the review and editing of the manuscript.

Data Availability Statement

The data that support the findings of this study are available from the corresponding author upon reasonable request.

Keywords

2D materials, capacitive deionization, electrochemical intercalation and exfoliation, exceptional volumetric capacity, nanolaminate membranes

Received: March 6, 2024

Revised: April 30, 2024

Published online: May 29, 2024

-
- [1] M. Rodell, J. S. Famiglietti, D. N. Wiese, J. T. Reager, H. K. Beaudoin, F. W. Landerer, M. H. Lo, *Nature* **2018**, *557*, 651.
- [2] S. Zhao, L. Zou, C. Y. Tang, D. Mulcahy, *J. Membr. Sci.* **2012**, *396*, 1.
- [3] R. Wang, L. Shi, C. Y. Tang, S. Chou, C. Qiu, A. G. Fane, *J. Membr. Sci.* **2010**, *355*, 158.
- [4] Y. Wang, Q. Pan, Y. Qiao, X. Wang, D. Deng, F. Zheng, B. Chen, J. Qiu, *Adv. Mater.* **2023**, *35*, 2210871.
- [5] H. Y. Yang, Z. J. Han, S. F. Yu, K. L. Pey, K. Ostrikov, R. Karnik, *Nat. Commun.* **2013**, *4*, 2220.
- [6] T. Y. Liu, J. Serrano, J. Elliott, X. Z. Yang, W. Cathcart, Z. X. Wang, Z. He, G. L. Liu, *Sci. Adv.* **2020**, *6*, eaaz0906.
- [7] S. Jeon, H.-r. Park, J.-g. Yeo, S. Yang, C. H. Cho, M. H. Han, D. K. Kim, *Energy Environ. Sci.* **2013**, *6*, 1471.
- [8] R. Ou, H. Zhang, V. X. Truong, L. Zhang, H. M. Hegab, L. Han, J. Hou, X. Zhang, A. Deletic, L. Jiang, G. P. Simon, H. Wang, *Nat. Sustain.* **2020**, *3*, 1052.
- [9] K. Zuo, X. Huang, X. Liu, E. M. Gil Garcia, J. Kim, A. Jain, L. Chen, P. Liang, A. Zepeda, R. Verduzco, J. Lou, Q. Li, *Environ. Sci. Technol.* **2020**, *54*, 13322.
- [10] J. G. Gamaethiralalage, K. Singh, S. Sahin, J. Yoon, M. Elimelech, M. E. Suss, P. Liang, P. M. Biesheuvel, R. L. Zornitta, L. C. P. M. de Smet, *Energy Environ. Sci.* **2021**, *14*, 1095.
- [11] J. Sun, S. Garg, T. D. Waite, *Environ. Sci. Technol.* **2023**, *57*, 14726.
- [12] M. Mao, T. Yan, J. Shen, J. Zhang, D. Zhang, *Environ. Sci. Technol.* **2021**, *55*, 7665.
- [13] M. Mao, T. Yan, G. Chen, J. Zhang, L. Shi, D. Zhang, *Environ. Sci. Technol.* **2021**, *55*, 730.
- [14] P. Simon, Y. Gogotsi, *Nat. Mater.* **2020**, *19*, 1151.
- [15] L. Wang, J. E. Dykstra, S. H. Lin, *Environ. Sci. Technol.* **2019**, *53*, 3366.
- [16] X. Xu, M. Eguchi, Y. Asakura, L. Pan, Y. Yamauchi, *Energy Environ. Sci.* **2023**, *16*, 1815.
- [17] S. Kumar, N. M. Aldaqqa, E. Alhseinat, D. Shetty, *Angew. Chem. Int. Ed.* **2023**, *62*, 202302180.
- [18] Z.-H. Huang, Z. Yang, F. Kang, M. Inagaki, *J. Mater. Chem. A* **2017**, *5*, 470.
- [19] H. Peng, B. Yao, X. Wei, T. Liu, T. Kou, P. Xiao, Y. Zhang, Y. Li, *Adv. Energy Mater.* **2019**, *9*, 1803665.
- [20] X. Xu, Y. Liu, T. Lu, Z. Sun, D. H. C. Chua, L. Pan, *J. Mater. Chem. A* **2015**, *3*, 13418.
- [21] H. Yin, S. Zhao, J. Wan, H. Tang, L. Chang, L. He, H. Zhao, Y. Gao, Z. Tang, *Adv. Mater.* **2013**, *25*, 6270.
- [22] S. Cao, Y. Li, Y. Tang, Y. Sun, W. Li, X. Guo, F. Yang, G. Zhang, H. Zhou, Z. Liu, Q. Li, M. Shakouri, H. Pang, *Adv. Mater.* **2023**, *35*, 2301011.
- [23] L. L. Zhang, X. S. Zhao, *Chem. Soc. Rev.* **2009**, *38*, 2520.
- [24] Y. Gogotsi, P. Simon, *Science* **2011**, *334*, 917.
- [25] Q. Li, X. Xu, J. Guo, J. P. Hill, H. Xu, L. Xiang, C. Li, Y. Yamauchi, Y. Mai, *Angew. Chem., Int. Ed.* **2021**, *60*, 26528.
- [26] A. B. Fuertes, G. Lota, T. A. Centeno, E. Frackowiak, *Electrochim. Acta* **2005**, *50*, 2799.
- [27] Y. Xia, T. S. Mathis, M. Q. Zhao, B. Anasori, A. Dang, Z. H. Zhou, H. Cho, Y. Gogotsi, S. Yang, *Nature* **2018**, *557*, 409.
- [28] X. Shen, Y. Xiong, R. Hai, F. Yu, J. Ma, *Environ. Sci. Technol.* **2020**, *54*, 4554.
- [29] W. S. Chen, J. J. Gu, Q. L. Liu, M. Z. Yang, C. Zhan, X. N. Zang, T. A. Pham, G. X. Liu, W. Zhang, D. Zhang, B. Dunn, Y. M. Wang, *Nat. Nanotechnol.* **2022**, *17*, 153.
- [30] F. Xing, T. Li, J. Li, H. Zhu, N. Wang, X. Cao, *Nano Energy* **2017**, *31*, 590.
- [31] V. Augustyn, Y. Gogotsi, *Joule* **2017**, *1*, 443.
- [32] L. Ding, L. Li, Y. Liu, Y. Wu, Z. Lu, J. Deng, Y. Wei, J. Caro, H. Wang, *Nat. Sustain.* **2020**, *3*, 296.
- [33] W. Wang, N. Onofrio, E. Petit, B. A. Karamoko, H. Wu, J. Liu, J. Li, K. Qi, Y. Zhang, C. Gervais, L. Lajaunie, C. Salameh, P. Miele, Z. Zeng, D. Voiry, *Nat. Water.* **2023**, *1*, 187.
- [34] L. Mei, Z. Cao, T. Ying, R. Yang, H. Peng, G. Wang, L. Zheng, Y. Chen, C. Y. Tang, D. Voiry, H. Wang, A. B. Farimani, Z. Zeng, *Adv. Mater.* **2022**, *34*, 2201416.
- [35] X. Zhao, S. Ning, W. Fu, S. J. Pennycook, K. P. Loh, *Adv. Mater.* **2018**, *30*, 1802397.
- [36] Z. Lai, Q. He, T. H. Tran, D. V. M. Repaka, D.-D. Zhou, Y. Sun, S. Xi, Y. Li, A. Chaturvedi, C. Tan, B. Chen, G.-H. Nam, B. Li, C. Ling, W. Zhai, Z. Shi, D. Hu, V. Sharma, Z. Hu, Y. Chen, Z. Zhang, Y. Yu, X. Renshaw Wang, R. V. Ramanujan, Y. Ma, K. Hippalgaonkar, H. Zhang, *Nat. Mater.* **2021**, *20*, 1113.
- [37] Y. Yu, G.-H. Nam, Q. He, X.-J. Wu, K. Zhang, Z. Yang, J. Chen, Q. Ma, M. Zhao, Z. Liu, F.-R. Ran, X. Wang, H. Li, X. Huang, B. Li, Q. Xiong, Q. Zhang, Z. Liu, L. Gu, Y. Du, W. Huang, H. Zhang, *Nat. Chem.* **2018**, *10*, 638.
- [38] M. Acerce, D. Voiry, M. Chhowalla, *Nat. Nanotechnol.* **2015**, *10*, 313.
- [39] Z. Zeng, Z. Yin, X. Huang, H. Li, Q. He, G. Lu, F. Boey, H. Zhang, *Angew. Chem., Int. Ed.* **2011**, *50*, 11093.
- [40] R. Yang, L. Mei, Q. Zhang, Y. Fan, H. S. Shin, D. Voiry, Z. Zeng, *Nat. Protoc.* **2022**, *17*, 358.
- [41] R. Yang, Y. Fan, L. Mei, H. S. Shin, D. Voiry, Q. Lu, J. Li, Z. Zeng, *Nat Synth* **2023**, *2*, 101.
- [42] J. N. Coleman, M. Lotya, A. O'Neill, S. D. Bergin, P. J. King, U. Khan, K. Young, A. Gaucher, S. De, R. J. Smith, I. V. Shvets, S. K. Arora, G. Stanton, H.-Y. Kim, K. Lee, G. T. Kim, G. S. Duesberg, T. Hallam, J. J. Boland, J. J. Wang, J. F. Donegan, J. C. Grunlan, G. Moriarty, A. Shmeliov, R. J. Nicholls, J. M. Perkins, E. M. Grievson, K. Theuwissen, D. W. McComb, P. D. Nellist, et al., *Science* **2011**, *331*, 568.
- [43] Z. Shi, X. Zhang, X. Lin, G. Liu, C. Ling, S. Xi, B. Chen, Y. Ge, C. Tan, Z. Lai, Z. Huang, X. Ruan, L. Zhai, L. Li, Z. Li, X. Wang, G.-H. Nam, J. Liu, Q. He, Z. Guan, J. Wang, C.-S. Lee, A. R. J. Kucernak, H. Zhang, *Nature* **2023**, *621*, 300.
- [44] L. Ries, E. Petit, T. Michel, C. C. Diogo, C. Gervais, C. Salameh, M. Bechelany, S. Balme, P. Miele, N. Onofrio, D. Voiry, *Nat. Mater.* **2019**, *18*, 1112.
- [45] M. E. Suss, S. Porada, X. Sun, P. M. Biesheuvel, J. Yoon, V. Presser, *Energy Environ. Sci.* **2015**, *8*, 2296.
- [46] X. Yang, C. Cheng, Y. Wang, L. Qiu, D. Li, *Science* **2013**, *341*, 534.
- [47] J. Han, T. Yan, J. Shen, L. Shi, J. Zhang, D. Zhang, *Environ. Sci. Technol.* **2019**, *53*, 12668.

- [48] C. Zhan, Y. Sun, F. Aydin, Y. M. Wang, T. A. Pham, *J. Chem. Phys.* **2021**, *154*, 164706.
- [49] G. Kresse, D. Joubert, *Phys. Rev. B* **1999**, *59*, 1758.
- [50] G. Kresse, J. Furthmüller, *Phys. Rev. B* **1996**, *54*, 11169.
- [51] G. Kresse, J. Furthmüller, *Comput. Mater. Sci.* **1996**, *6*, 15.
- [52] J. P. Perdew, K. Burke, M. Ernzerhof, *Phys. Rev. Lett.* **1996**, *77*, 3865.
- [53] P. E. Blöchl, *Phys. Rev. B* **1994**, *50*, 17953.
- [54] S. Grimme, *J. Comput. Chem.* **2006**, *27*, 1787.
- [55] K. Mathew, R. Sundararaman, K. Letchworth-Weaver, T. A. Arias, R. G. Hennig, *J. Chem. Phys.* **2014**, *140*, 084106.
- [56] K. Mathew, V. S. C. Kolluru, S. Mula, S. N. Steinmann, R. G. Hennig, *J. Chem. Phys.* **2019**, *151*, 234101.